

1 Mapping yearly fine resolution global surface ozone  
2 through the Bayesian Maximum Entropy data fusion  
3 of observations and model output for 1990–2017

4 Marissa N. DeLang<sup>1</sup>, Jacob S. Becker<sup>1</sup>, Kai-Lan Chang<sup>2,3</sup>, Marc L. Serre<sup>1</sup>, Owen R. Cooper<sup>2,3</sup>,  
5 Martin G. Schultz<sup>4</sup>, Sabine Schröder<sup>4</sup>, Xiao Lu<sup>5</sup>, Lin Zhang<sup>5</sup>, Makoto Deushi<sup>6</sup>, Beatrice Josse<sup>7</sup>,  
6 Christoph A. Keller<sup>8,9</sup>, Jean-François Lamarque<sup>10</sup>, Meiyun Lin<sup>11,12</sup>, Junhua Liu<sup>8,9</sup>, Virginie  
7 Marécal<sup>7</sup>, Sarah A. Strode<sup>8,9</sup>, Kengo Sudo<sup>13,14</sup>, Simone Tilmes<sup>10</sup>, Li Zhang<sup>11,12,15</sup>, Stephanie E.  
8 Cleland<sup>1</sup>, Elyssa L. Collins<sup>1</sup>, Michael Brauer<sup>16,17</sup>, J. Jason West<sup>\*,1</sup>

9 <sup>1</sup>Department of Environmental Sciences and Engineering, University of North Carolina at Chapel Hill, Chapel Hill,  
10 NC, USA

11 <sup>2</sup>Cooperative Institute for Research in Environmental Sciences, University of Colorado, Boulder, CO, USA

12 <sup>3</sup>NOAA Chemical Sciences Laboratory, Boulder, CO, USA

13 <sup>4</sup>Jülich Supercomputing Centre (JSC), Forschungszentrum Jülich, Jülich, Germany

14 <sup>5</sup>Laboratory for Climate and Ocean-Atmosphere Studies, Department of Atmospheric and Oceanic Sciences, School  
15 of Physics, Peking University, Beijing, China

16 <sup>6</sup>Meteorological Research Institute (MRI), Tsukuba, Japan

17 <sup>7</sup>Centre National de Recherches Météorologiques, Université de Toulouse, Météo-France, CNRS, Toulouse, France

18 <sup>8</sup>NASA Goddard Space Flight Center, Greenbelt, MD, USA

19 <sup>9</sup>Universities Space Research Association, Columbia, MD, USA

20 <sup>10</sup>National Center for Atmospheric Research, Boulder, CO, USA

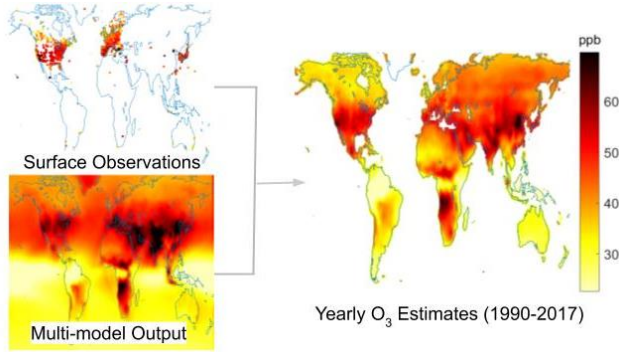
21 <sup>11</sup>NOAA Geophysical Fluid Dynamics Laboratory, Princeton, NJ, USA

22 <sup>12</sup>Program in Atmospheric and Oceanic Sciences, Princeton University, Princeton, NJ, USA

23 <sup>13</sup>Graduate School of Environmental Studies, Nagoya University, Nagoya, Japan

- 24 <sup>14</sup>Japan Agency for Marine-Earth Science and Technology (JAMSTEC), Yokosuka, Japan
- 25 <sup>15</sup>Department of Meteorology and Atmospheric Science, Pennsylvania State University, University Park, PA. USA
- 26 <sup>16</sup>Institute for Health Metrics and Evaluation, University of Washington, Seattle, Washington, USA
- 27 <sup>17</sup>School of Population and Public Health, University of British Columbia, Vancouver, British Columbia, Canada

28 **TOC GRAPHIC**



29

30 **ABSTRACT**

31 Estimates of ground-level ozone concentrations are necessary to determine the human  
32 health burden of ozone. To support the Global Burden of Disease Study, we produce yearly fine  
33 resolution global surface ozone estimates from 1990 to 2017 through a data fusion of  
34 observations and models. As ozone observations are sparse in many populated regions, we use a  
35 novel combination of the M<sup>3</sup>Fusion and Bayesian Maximum Entropy (BME) methods. With  
36 M<sup>3</sup>Fusion, we create a multi-model composite by bias-correcting and weighting nine global  
37 atmospheric chemistry models based on their ability to predict observations (8,834 sites globally)  
38 in each region and year. BME is then used to integrate observations, such that estimates match  
39 observations at each monitoring site with the observational influence decreasing smoothly across  
40 space and time until the output matches the multi-model composite. After estimating at 0.5°  
41 resolution using BME, we add fine spatial detail from an additional model, yielding estimates at  
42 0.1° resolution. Observed ozone is predicted more accurately ( $R^2=0.81$  at test point, 0.63 at 0.1°,  
43 0.62 at 0.5°) than the multi-model mean ( $R^2=0.28$  at 0.5°). Global ozone exposure is estimated to  
44 be increasing, driven by highly populated regions of Asia and Africa, despite decreases in the  
45 United States and Russia.

46

47 **INTRODUCTION**

48           Tropospheric ozone is harmful to human health through respiratory and cardiovascular  
49 health effects associated with short and long term exposure.<sup>1-3</sup> Additionally, tropospheric ozone  
50 influences climate<sup>3</sup> and damages plant growth.<sup>5,6</sup> Surface ozone estimates at fine spatial  
51 resolution, which are required to determine the human health burden of ozone exposure, are  
52 typically based on two sources: monitoring networks and atmospheric chemistry models.  
53 Monitoring networks provide high spatial coverage of surface ozone observations in North  
54 America, Europe, Japan, South Korea, and recently China; however, stations are scarce  
55 elsewhere.<sup>7</sup> Global atmospheric models provide concentration estimates across many years and  
56 cover all world regions; however, models have biases.<sup>8</sup>

57           The Global Burden of Disease (GBD) Study conducts a comparative risk assessment that  
58 estimates the health burden caused by specific risk factors from 1990 to present day, updated  
59 regularly. Two ambient air pollution risk factors are analyzed: fine particulate matter (PM<sub>2.5</sub>) and  
60 ozone.<sup>9,10</sup> GBD PM<sub>2.5</sub> estimates are generated through a combination of satellite retrievals and  
61 land use information with a single atmospheric model calibrated to surface observations with a  
62 Bayesian hierarchical model.<sup>11,12</sup> In contrast, global ozone estimates prior to GBD 2017<sup>13</sup> were  
63 provided by a single model with no bias correction to observations.<sup>14</sup> Satellite measurements  
64 provide PM<sub>2.5</sub> estimates at fine resolution, but do not accurately detect surface ozone.<sup>14,15</sup>

65           The recent Tropospheric Ozone Assessment Report (TOAR) collected ozone  
66 observations from thousands of sites around the world, which made it possible to incorporate  
67 surface observations into GBD estimates.<sup>7,16</sup> For GBD 2017, TOAR observations were combined  
68 with six atmospheric models from phase one of the Chemistry-Climate Model Initiative  
69 (CCMI)<sup>17</sup> using the M<sup>3</sup>Fusion method for the average of 2008 to 2014.<sup>18</sup> In M<sup>3</sup>Fusion, the

70 models were bias corrected and combined by finding the optimal linear combination of models in  
71 each world region, weighted based on their performance with respect to observations. Within  
72 two degrees of a monitoring station, the multi-model composite was then replaced with a spatial  
73 interpolation of observations. The 2008–2014 ozone distribution was extended backwards  
74 (1990–2008) by scaling with cubic splines relative to prior GBD ozone estimates and forwards  
75 (2014–2017) by extending the annual rate of change from 2012, for use in GBD 2017.<sup>13</sup>

76 While the M<sup>3</sup>Fusion method significantly improved upon previous GBD ozone estimates,  
77 we identify a potential for further improvements. In particular, the correction within two degrees  
78 of an observation can create discontinuities, which could be improved by using advanced  
79 geostatistical techniques that combine model output with observations using smooth weighting  
80 across space. Here we use a novel combination of the M<sup>3</sup>Fusion and Bayesian Maximum  
81 Entropy (BME) methods,<sup>19-22</sup> which is uniquely suited to the challenges of mapping global ozone  
82 concentrations, as only observations and models provide useful information and observations are  
83 sparse in some world regions. The regional “large-scale” bias correction and weighting of  
84 models in the M<sup>3</sup>Fusion multi-model composite provides the best estimate of ozone far from  
85 observations. Then BME provides a local “small-scale” correction, by smoothly integrating  
86 observations in both space and time such that estimates match observations at the measurement  
87 site, and the influence of those observations decreases with distance according to the  
88 spatiotemporal covariance. Since ozone monitoring is inconsistent, allowing observations to  
89 affect predictions across time could provide more accurate estimates. Near observation locations,  
90 therefore, ozone estimates will be strongly influenced by observations. BME has previously  
91 been used to fuse ozone observations with models on state and national scales,<sup>23-25</sup> but it has not  
92 been used previously globally, and apart from Chang et al.,<sup>18</sup> we are not aware of any global data

93 fusion of ozone observations and models.

94 We aim to estimate global fine resolution (0.1°) surface ozone for each year from 1990 to  
95 2017 to support the GBD 2019 Study by combining surface observations with multiple global  
96 atmospheric models by first using M<sup>3</sup>Fusion to create multi-model composites, and then  
97 applying BME to smoothly fuse multi-model composites with observations in space and time.  
98 We improve upon the single 7-year mean ozone fields produced for GBD 2017<sup>18</sup> by producing  
99 yearly output for 1990-2017, including additional observations and model output, smoothly  
100 weighting observations across space and time, and applying fine spatial structure based on fine  
101 resolution model output. To add fine spatial resolution for GBD, we apply the fine-scale spatial  
102 patterns from a global fine resolution model simulation.<sup>26</sup> Our annual global ozone maps were  
103 used by GBD 2019, which extrapolated to 2019 using log-linear trends based on our 2008-2017  
104 estimates, and estimated 365,000 (95% CI: 175,000-564,000) premature chronic obstructive  
105 pulmonary disease deaths globally, or 6.21 (2.99-9.63) million disability adjusted life years, from  
106 ambient ozone exposure in 2019.<sup>27</sup>

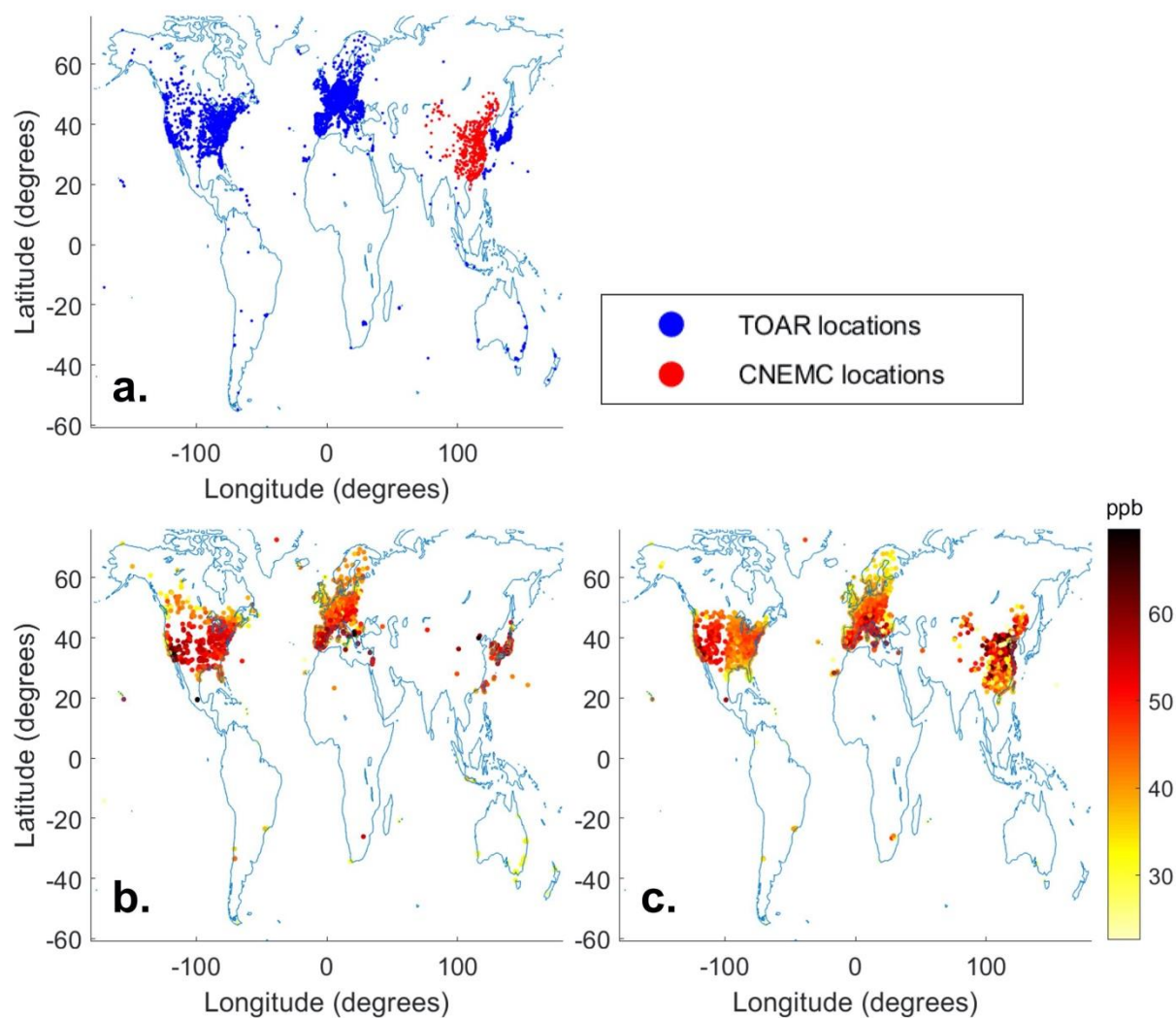
## 107 **MATERIALS AND METHODS**

108 M<sup>3</sup>Fusion and BME are used in sequence to estimate global surface ozone  
109 concentrations. Other methods have been applied on smaller scales, such as neural networks  
110 using meteorological and emission variables to predict ozone,<sup>28,29</sup> but those relationships may not  
111 apply elsewhere, and those methods are inappropriate where there are no observations.

112 GBD's ozone metric for quantifying health outcomes from long term ozone exposure is  
113 the ozone season daily maximum 8-hour mixing ratio (OSDMA8).<sup>2</sup> OSDMA8 is calculated as  
114 the annual maximum of the six-month running mean of the monthly average daily maximum 8-  
115 hour mixing ratio, including months through March of the following year to contain the Southern

116 Hemisphere summer. All observations, model output, and estimates are reported here as  
117 OSDMA8.

118 ***Surface Ozone Observations.*** We include surface ozone observations from TOAR and the  
119 Chinese National Environmental Monitoring Center (CNEMC) Network (Figure 1). TOAR is the  
120 world's largest collection of in-situ hourly surface ozone observations covering 1970-2015.<sup>16,30</sup>  
121 The database contains dense observations in North America, Europe, Japan, and South Korea,  
122 and sparse observations elsewhere.<sup>7</sup> The database was updated for this project to include readily-  
123 available datasets for the years 2015–2017, but measurements were not updated for all nations  
124 previously included. CNEMC includes surface ozone observations for 2013–2017 in China,<sup>31</sup>  
125 which were quality-controlled using the same algorithm that TOAR applies elsewhere. The total  
126 observations ranged from a minimum of 1,199 in 1990 to a maximum of 4,999 in 2015. The  
127 incomplete TOAR update in 2016 and 2017 yielded fewer observation sites than 2015.



128

129 **Figure 1.** (a) TOAR and CNEMC monitoring locations with at least one valid yearly OSDMA8  
 130 observation over 1990–2017. In total, there are 8,834 monitoring stations, 7,269 from TOAR and  
 131 1,565 from CNEMC. (b) Surface observations as OSDMA8 in 2005, with an average of 45.5 ppb  
 132 and maximum of 82.2 ppb in Mexico City, Mexico. (c) Surface observations as OSDMA8 in  
 133 2015, with an average of 46.2 ppb and maximum of 80.9 ppb in Zibo, China.

134 **Atmospheric Chemistry Model Simulations.** We incorporate modeled ozone from nine  
 135 atmospheric chemistry model simulations (Table 1). The models, mostly from CCMI,<sup>17</sup> report  
 136 output for 1990–2010 from the specified dynamics REF-C1SD experiment,<sup>17,32</sup> which uses



137 annual MACCity emissions .<sup>33,34</sup> Three models, MOCAGE, MERRA2-GMI, and GFDL-AM3,  
 138 were extended past 2010. To increase models after 2010, we include output from the specified  
 139 dynamics experiments of MRI-ESM2.0 and GFDL-AM4, for modified Coupled Model  
 140 Intercomparison Project Phase 6 (CMIP6)<sup>35</sup> experiments. Hourly ozone mixing ratios were  
 141 processed to OSDMA8, using the same algorithm as for observations.

142 **Table 1.** Nine atmospheric chemistry models used in this study.

Model	Years	Resolution	Experiment	Reference
CESM1 CAM4-Chem	1990–2010	1.9° × 2.5°	CCMI REF-C1SD	36
CESM1 WACCM	1990–2010	1.9° × 2.5°	CCMI REF-C1SD	37,38
CHASER	1990–2010	2.8° × 2.8°	CCMI REF-C1SD	39-41
GFDL AM3	1990–2014	2° × 2.5°	CCMI REF-C1SD	42-44
GFDL AM4	2010–2016	1° × 1.25°	CMIP6 nudged to NCEP winds <sup>a</sup>	45,46
MERRA2-GMI	1990–2017	0.5° × 0.625°	MACCity and GFED-4s emissions <sup>b</sup>	47,48
MOCAGE	1990–2016	2° × 2°	CCMI REF-C1SD	49,50
MRI-ESM1r1	1990–2010	2.8° × 2.8°	CCMI REF-C1SD	51
MRI-ESM2.0	2011–2017	2.8° × 2.8°	CMIP6 historical and ssp370 <sup>c</sup>	452

143 <sup>a</sup> Nudged to observed meteorology similar to GFDL-AM3 and uses anthropogenic emissions modified from CMIP6  
 144 to reflect recent NO<sub>x</sub> trends in China and the United States<sup>45</sup>

145 <sup>b</sup> MACCity anthropogenic emissions with biomass burning emissions from Global Fire Emissions Dataset version  
 146 4s<sup>47,48</sup>

147 <sup>c</sup> Emissions from the CMIP6 historical (2011–2014) and ssp370 (2015–2017) experiments<sup>52</sup>

148 **Multi-model Composite.** We use M<sup>3</sup>Fusion to create multi-model composites of the models  
 149 available in each year from 1990–2017.<sup>18</sup> This method corrects for model bias and finds the

150 linear combination of models in each region and year that minimizes the mean square error as  
 151 compared to observations. Since model resolution varies, we use bilinear interpolation to smooth  
 152 yearly OSDMA8 to a  $0.5^\circ \times 0.5^\circ$  grid. We interpolate yearly observations from irregular  
 153 monitoring station locations to the  $0.5^\circ$  grid using the stochastic partial differential equation  
 154 approach.<sup>53</sup> In each of eight geographical regions (Figure S1) and each year, we weight each  
 155 model to minimize the difference between the multi-model average and spatially interpolated  
 156 observations based on a constrained least squares approach:

$$\begin{aligned}
 & \text{minimize} \\
 & \{\alpha_r, \beta_{rk}; k = 1, \dots, n\} \sum_{s_g \in \text{Region } r} (\hat{y}(s_g) - \alpha_r - \sum_{k=1}^n \beta_{rk} \eta_k(s_g))^2, \quad (1) \\
 & \text{subject to } \sum_{k=1}^n \beta_{rk} = 1 \text{ and } \beta_{rk} \geq 0
 \end{aligned}$$

159 where  $s_g$  is the grid cell at  $0.5^\circ$  resolution,  $\hat{y}(s_g)$  is the spatially interpolated observations,  $\{\eta_k(s_g);$   
 160  $k=1, \dots, n\}$  is the model output on the same grid from the  $n$  models available,  $\alpha_r$  is a constant that  
 161 corrects overall bias in each region, and  $\beta_{rk}$  is an optimal weight for the  $k$ -th model in region  $r$ .  
 162 All model weights are constrained to be positive and sum to 1. The constant offset  $\alpha_r$  guarantees  
 163 that the residuals from this optimization have a zero mean, through which the mean model bias is  
 164 corrected in each region.<sup>18</sup>

165 Since M<sup>3</sup>Fusion relies on spatially interpolated observations to determine model weights,  
 166 we modify the method for data sparse regions and years. In North America and Europe, we use  
 167 weights based on each individual year's models and observation values. For all other regions, we  
 168 calculate individual year weights for 2000–2010, and apply weights from the aggregated 2000–  
 169 2010 period to 1990–1999. For 2011–2017, East Asia uses individual year weights, while South  
 170 America, Africa, South-Central Asia, Russia, and Oceania use weights from the aggregated

171 2011–2014 period, for which the TOAR dataset was complete.

172 **Bayesian Maximum Entropy Methodology.** BME is a geostatistical method that incorporates  
173 multiple forms of knowledge to predict an estimate of a homogenous, stationary, space-time  
174 random field.<sup>19-22</sup> Using BME, we combine surface observations and annual multi-model  
175 composites to calculate an ozone estimate that matches observations at each monitoring station  
176 and the observational influence gradually diminishes across space and time until it matches the  
177 multi-model composite. BME has been described previously, including in the fusion of ozone  
178 observations with model output at state and national scales<sup>120-24,54</sup>. We model the offset-  
179 removed, homogeneous space-time random field (S/TRF)  $X(\mathbf{p})$  at the space-time coordinate  
180  $\mathbf{p}=(s,t)$ .<sup>24</sup> In BME, there are two forms of knowledge: site-specific and general. Site-specific  
181 knowledge can consist of hard data, with no assumed uncertainty, and soft, probabilistic data.  
182 Here we only have hard data, which is the linear limiting case of the BME data integration  
183 framework.<sup>24</sup> We remove the offset, the multi-model composite at monitoring stations ( $o_z(\mathbf{p}_0)$ ),  
184 from OSDMA8 observations ( $\mathbf{z}_0$ ) at monitoring station locations  $\mathbf{p}_0$  to obtain hard data  $\mathbf{x}_0$ :

$$185 \quad \mathbf{x}_0 = \mathbf{z}_0 - o_z(\mathbf{p}_0) \quad (2)$$

186 The general knowledge base of  $X(\mathbf{p})$  includes the mean function  $m_x(\mathbf{p}) = E[X]$ , which is assumed  
187 to be zero, and the covariance function  $c_x(\mathbf{p},\mathbf{p}') = E[(X(\mathbf{p})-m(\mathbf{p}))(X(\mathbf{p}')-m(\mathbf{p}'))]$ , which is  
188 determined by the experimental covariance of  $\mathbf{x}_0$ :

$$189 \quad \widehat{c}_X(r, \tau) \approx \frac{1}{N(r,\tau)} \sum_{i=1}^{N(r,\tau)} x_{head,i} x_{tail,i} - m_X^2 \quad (3)$$

190 where  $N(r, \tau)$  is the number of pairs of points with values  $(x_{head}, x_{tail})$  separated by a distance  $r$   
191 and time  $\tau$ , and  $m_x$  is the mean of  $\mathbf{x}_0$ . For the S/TRF  $X(\mathbf{p})$ , we use an exponential covariance

192 model to best fit the experimental covariance:

$$193 \quad c_X(r, \tau) = C \left[ \gamma \exp \frac{-3r}{a_{r1}} \exp \frac{-3\tau}{a_{t1}} + \lambda \exp \frac{-3r}{a_{r2}} \exp \frac{-3\tau}{a_{t2}} + (1 - \gamma - \lambda) \exp \frac{-3r}{a_{r3}} \exp \frac{-3\tau}{a_{t3}} \right] \quad (4)$$

194 with parameters in the supporting information. The BME estimation process involves using  
195 general knowledge to obtain the maximum entropy prior probability density function (PDF) of  
196  $f_G$ , updating  $f_G$  by integrating site-specific knowledge to obtain the epistemic Bayesian posterior  
197 PDF  $f_K$ , which provides a complete stochastic description of  $X_k=X(\mathbf{p}_k)$  at the estimation point  $\mathbf{p}_k$ ,  
198 and computing space-time estimates based on  $f_K$ . The posterior PDF is defined as:

$$199 \quad f_K(x_k) = \left( \frac{f_G(x_0, x_k)}{f_G(x_0)} \right) \quad (5)$$

200 where  $x_k$  is the offset-removed estimate at points  $\mathbf{p}_k$ . We define the ozone space-time random  
201 field (S/TRF),  $Z(\mathbf{p})$ , as the sum of  $X(\mathbf{p})$  and the offset (multi-model composite):

$$202 \quad Z(\mathbf{p}) = X(\mathbf{p}) + o_z(\mathbf{p}) \quad (6)$$

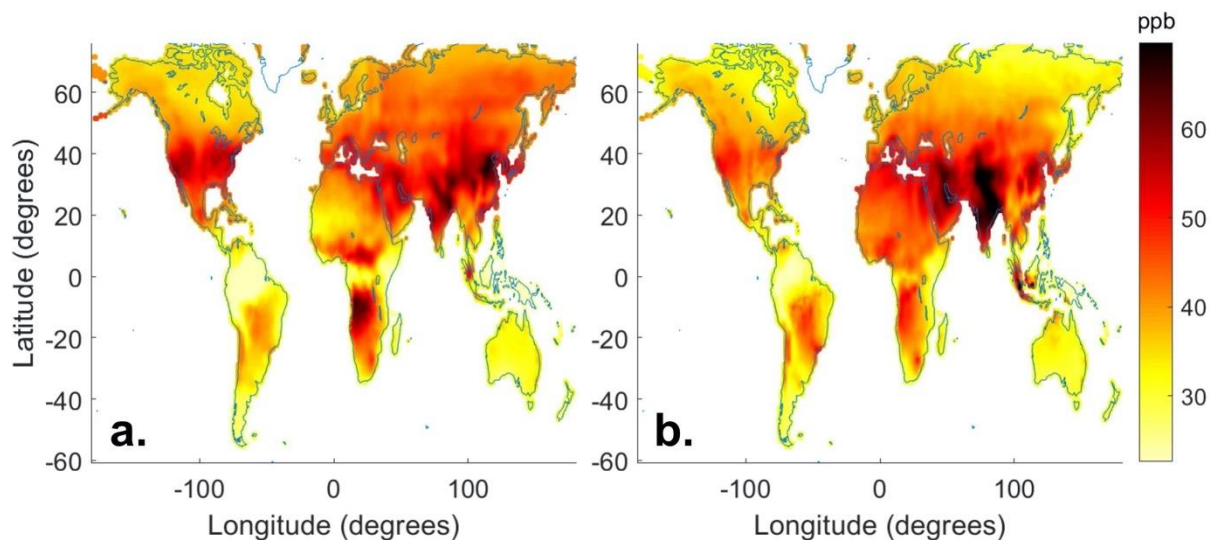
203 We obtain the estimated OSDMA8  $z_k$  at  $\mathbf{p}_k$  by obtaining the BME estimate  $x_k$  for the S/TRF  $X(\mathbf{p})$   
204 at  $\mathbf{p}_k$ , and adding back  $o_z(\mathbf{p}_k)$ .

205 ***Fine Resolution Addition.*** We calculate ozone BME estimates at  $0.5^\circ$  resolution; however, a  
206 finer resolution is desirable for GBD to reduce spatial misalignment with population. Since  
207 neither the observations nor the models represent ozone at fine resolution, except where  
208 observations are dense, we use the spatial distribution of a fine resolution model. We use output  
209 from a NASA G5NR-Chem model<sup>26</sup> simulation from July 2013 to June 2014 at  $0.125^\circ$   
210 resolution, which we regrid to  $0.1^\circ$  resolution, to provide the fine spatial structure within each  
211  $0.5^\circ$  grid cell for each year 1990-2017. While we do not expect the modeled 2013–2014 ozone to

212 be accurate for every year, we use the modeled spatial distribution to inform the fine-scale spatial  
213 pattern for each year. In doing so, we assume that the fine spatial patterns of OSDMA8 do not  
214 change over time, as these reflect the spatial distributions of emissions and land use, as well as  
215 influences like topography and land/water interfaces. For each 0.5° grid cell, we subtract the  
216 average of NASA G5NR-Chem grid cells from the BME estimate, and add this difference to  
217 each NASA G5NR-Chem grid cell at 0.1° to obtain our BME estimate at 0.1°. Consequently, the  
218 sub-grid variability of the output matches the G5NR-Chem model, and the average of each 0.5°  
219 grid cell remains the same as the BME estimate (Figures S2-3).

## 220 RESULTS

221 **Multi-model Composite.** We determine weights for each model in each region and year (Table  
222 S1). In most regions and years, the multi-model mean ozone (the simple average of all models) is  
223 biased high, as models generally overpredict ozone.<sup>8,18</sup> Therefore, the M<sup>3</sup>Fusion multi-model  
224 composite (Figure 2) tends to decrease average ozone compared to the multi-model mean.

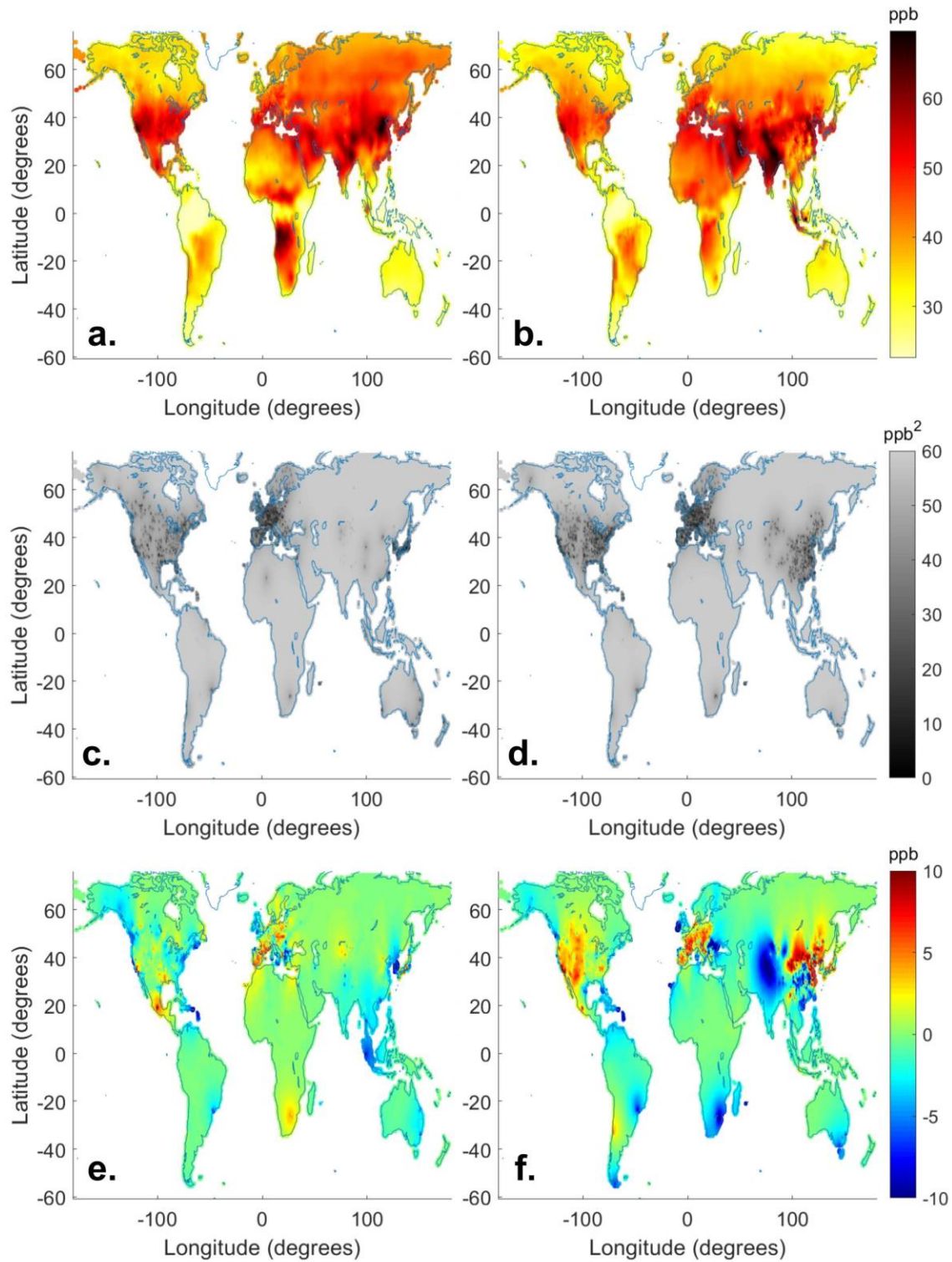


225  
226 **Figure 2.** Multi-model composite as OSDMA8 in 2005 (a) and 2015 (b).

227 **BME Coarse Resolution Output.** We obtain yearly ozone output at 0.5° resolution, with an

228 associated variance at each estimation point (Figure 3; Figures S4-31). The ozone output matches  
229 an observation at its space-time location, and the observation's influence decreases in space and  
230 time according to the derived spatiotemporal covariance (Equation S3). In regions with high  
231 observational coverage, there is greater spatial variation in our output, whereas less monitored  
232 regions are smoother. Across the years, areas of low estimated ozone include the Amazon,  
233 Oceania, and southeastern Africa; while high ozone is estimated in East Asia, South-Central  
234 Asia, western North America, and central Africa. The Amazon and central Africa are  
235 unmonitored; therefore, their respective low and high ozone estimates are based on model output  
236 reflecting ozone chemical destruction and dry deposition over the Amazon<sup>55</sup> and biomass  
237 burning in Africa.<sup>56</sup>

238 In BME, observations are treated as hard data with no variance; therefore, regions with the  
239 highest number of observations have the lowest variance, such as North America, Europe, and  
240 Japan in 2005 and additionally eastern China in 2015. Away from observations, the output is  
241 equal to the multi-model composite and the variance reaches a maximum of 60 ppb<sup>2</sup>, equal to the  
242 variance of the offset removed observations. To visualize how BME adjusted the multi-model  
243 composite using observations, we subtract the multi-model composite from our BME estimate  
244 (Figure 3). In unmonitored regions, there is no difference between our BME output and the  
245 multi-model composite. When adding fine resolution in the final step, differences on the global  
246 scale are unnoticeable (Figures S4-31).



247

248 **Figure 3.** BME estimate as OSDMA8 for 2005 (a) and 2015 (b). BME variance for 2005 (c) and

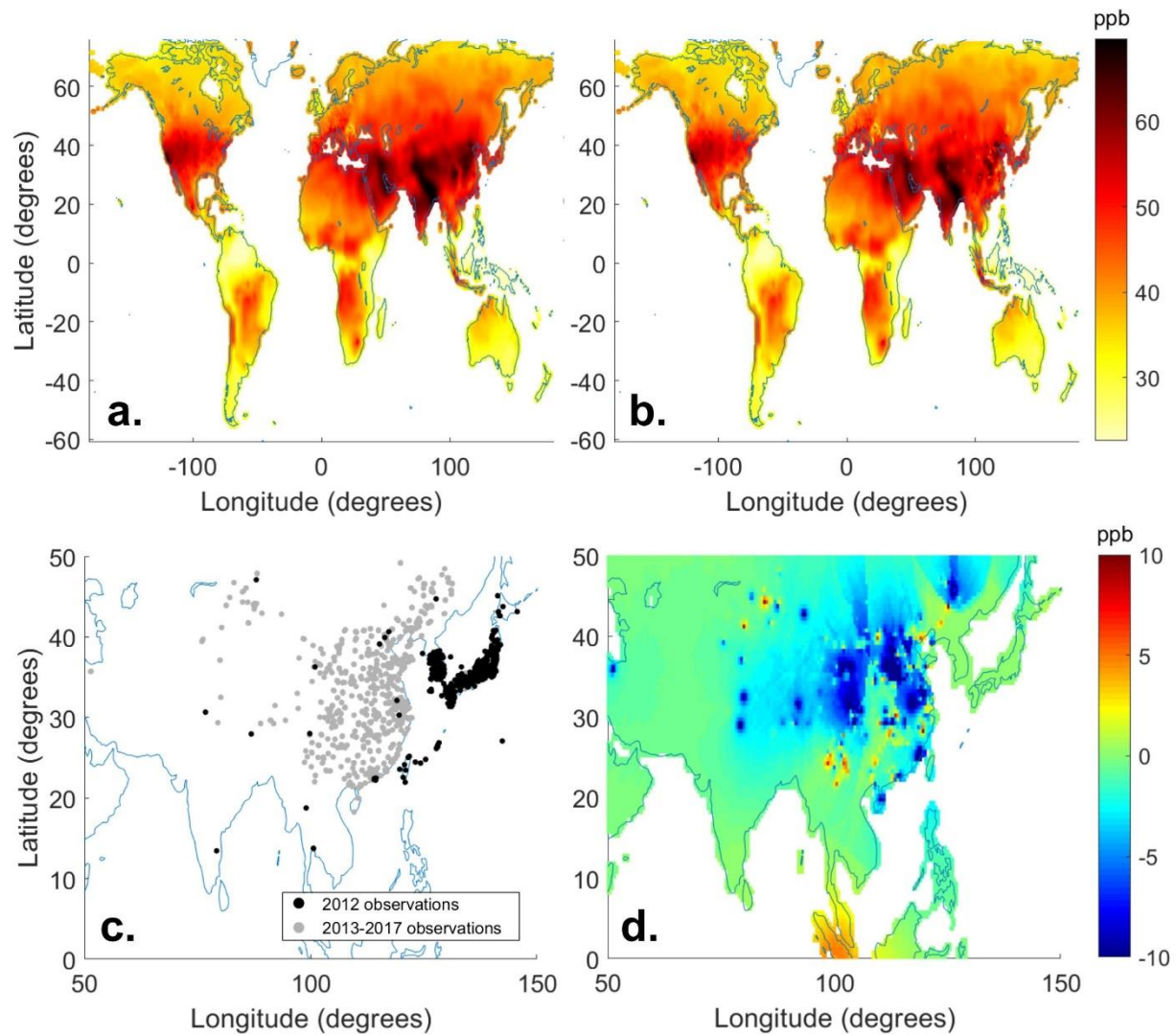
249 2015 (d). Effect of BME fusion of observations (BME estimate minus multi-model composite)

250 for 2005 (e) and 2015 (f). Positive values occur where our estimate is higher than the multi-  
251 model composite, negative values where our estimate is lower.

252 ***Influence of Observations through Time.*** The ability of an observation to influence other years  
253 is an important component of our method, since observational coverage changes, generally with  
254 more stations being added. The extent of an observation’s influence on other years depends on  
255 the number of nearby stations in space and time, with more remote stations having a longer  
256 temporal influence. In addition to the space-time BME estimates above, we also perform “space-  
257 only” BME, in which observations only influence ozone estimates across space in a single year.

258 By taking the difference between space-time and space-only results, we evaluate how  
259 observations influence other years. Since the CNEMC observations started in 2013, analyzing  
260 2012 highlights their temporal influence (Figure 4). On the global scale, the differences between  
261 the space-time and space-only methods are difficult to distinguish, but the major differences  
262 occur across China. Most of the non-zero differences occur in areas where CNEMC observations  
263 were added in 2013–2017, showing the influences of those observations (Figure 4). Whereas  
264 Figure 4 shows that BME largely decreased ozone estimates over China in 2012, the effect of  
265 adding BME differed among years, including increasing ozone in 2015 and 2016 (Figures S29-  
266 30).





267

268 **Figure 4.** (a) Space-only BME result in 2012 as OSDMA8. (b) Space-time BME result in 2012

269 as OSDMA8. (c) Observation locations in 2012 and 2013–2017. (d) Effect of BME space-time

270 influence of observations (space-time BME minus the space-only BME) for 2012.

271 **Evaluation.** To evaluate our results, we perform a leave one out cross validation (LOOCV),

272 where one observation is removed and we evaluate our ability to predict this observation, in five

273 scenarios:

274 - Multi-model mean: average of all model output available in a given year.

275 - Multi-model composite: combination of model output using M<sup>3</sup>Fusion.

- 276 - Space-only correction: BME corrected multi-model composite where observations  
277 only influence across space in a single year.
- 278 - Space-time correction: BME corrected multi-model composite where observations  
279 influence across space and time.
- 280 - Fine resolution: space-time corrected output with fine resolution from the NASA  
281 G5NR-Chem model.

282 LOOCV was performed using two methods: predicting ozone at the test point's grid cell and at  
283 the test point's specific space-time location. The grid cell prediction was performed to allow a  
284 fair comparison between scenarios, since the fine resolution addition is limited to predicting at  
285 the grid cell level, and to evaluate the benefit of increasing output resolution. When predicting at  
286 the test point's grid cell, each subsequent scenario improved performance, as shown by the root  
287 mean square error (RMSE) (Table 2). The multi-model composite outperforms the multi-model  
288 mean across all validation statistics. Correcting the multi-model composite across space using  
289 observations improves the results, which is further amplified by correcting across both space and  
290 time. Adding fine spatial structure, which gives our final output, slightly improves performance  
291 relative to the space-time scenario. All methods overestimate ozone in comparison to  
292 observations, as shown by the mean error (Table 2), though our final product is biased high only  
293 slightly.

294 **Table 2.** LOOCV statistics,<sup>a</sup> where results are evaluated in the 0.5 or 0.1 grid cells containing the  
 295 test point, or at the test point’s space-time location.

Scenario	Prediction location	RMSE (ppb)	ME (ppb)	R <sup>2</sup>	varE (ppb <sup>2</sup> )	varZ (ppb <sup>2</sup> )
Multi-model Mean	0.5° grid cell	13.76	11.00	0.28	68.48	62.08
Multi-model Composite	0.5° grid cell	7.82	1.05	0.30	60.03	43.09
Space-only Correction	0.5° grid cell	6.01	0.42	0.57	36.00	60.14
Space-time Correction	0.5° grid cell	5.62	0.57	0.62	31.30	62.01
Fine Resolution	0.1° grid cell	5.54	0.22	0.63	30.68	63.24
Multi-model Composite	Test point’s location	7.82	1.07	0.30	60.00	43.19
Space-time Correction	Test point’s location	3.99	0.01	0.81	15.94	81.26

296 <sup>a</sup>Root mean square error (RMSE), mean error (ME), R-squared (R<sup>2</sup>), variance of error (varE), and variance of the  
 297 estimated ozone (varZ). The mean and variance of observed ozone are mO=45.62 ppb and varO=81.96 ppb<sup>2</sup>,  
 298 respectively. Statistic definitions are included in Table S2.

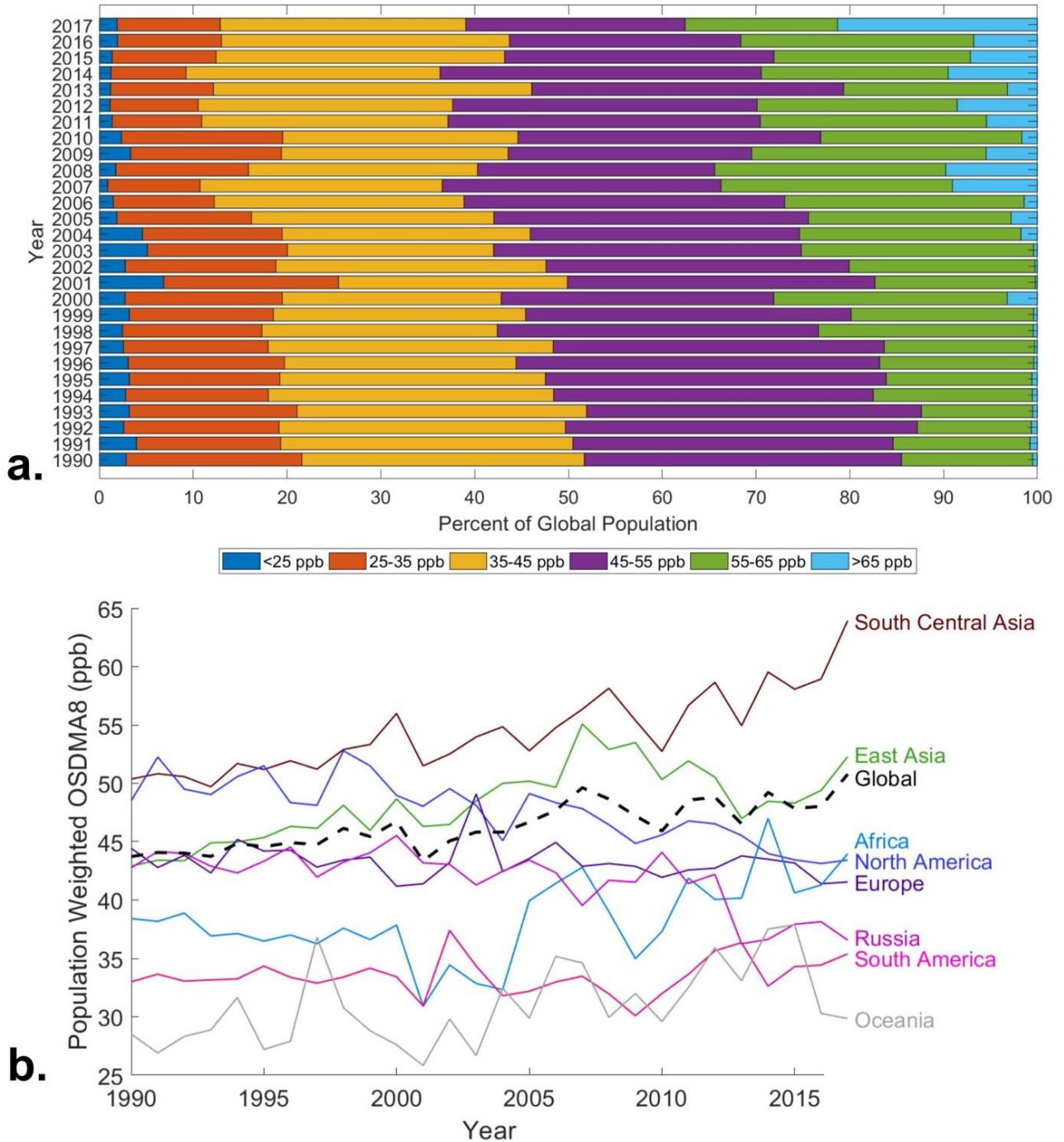
299  
 300 For comparison with other studies, we include statistics for predicting at the specific  
 301 space-time location (Table 2). The addition of the space-time correction to the multi-model  
 302 composite decreased RMSE from 7.82 to 3.99 ppb, a 49% reduction. In comparison, Chang et  
 303 al.<sup>18</sup> report that the correction to the multi-model composite in that study decreased the RMSE  
 304 from 5.16 to 3.82 ppb, a 26% reduction. The greater relative reduction in RMSE here is  
 305 attributed to the incorporation of both spatial and temporal autocorrelation, and shows our  
 306 improvement relative to Chang et al.<sup>18</sup>.

307 **Population-Weighted Ozone Trends.** With our yearly output, we use global gridded population  
 308 from GBD 2019 to analyze trends in population-weighted ozone as an indicator of exposure. The

309 2019 global population is used for all years, meaning that differences in exposure result from  
310 changes in ozone, not population. To determine how ozone exposure has changed from 1990–  
311 2017, we examine the percent of the global population exposed to intervals of OSDMA8 (Figure  
312 5). Global ozone exposure increases over this period, with an increase in the global population  
313 exposed to highest concentrations (>55 ppb). In 2017, 21.3% of the global population was  
314 exposed to OSDMA8 higher than 65 ppb, more than double the percentage in any previous year.  
315 Note that the OSDMA8 metric is not compared easily with national standards or WHO  
316 guidelines, which are typically based on the daily 8-hr maximum. For perspective, the risk of all-  
317 cause, circulatory, and respiratory mortality reportedly increases by 2%, 3%, and 12% per 10 ppb  
318 increase in long-term OSDMA8, respectively, with some evidence that ozone influences  
319 mortality at concentrations above about 35 ppb.<sup>2</sup>

320 We analyze the population-weighted trends from 1990–2017 for each world region  
321 (Figure 5) and the most populous countries (Figure S32). Globally, there is a positive trend in  
322 population weighted ozone for 1990–2017, driven in large part by positive trends in highly  
323 populated and polluted regions of South-Central Asia, East Asia, and Africa. Low population-  
324 weighted ozone occurs in South America and Oceania. Negative trends occur in North America  
325 and Russia; Europe has a weak negative trend, with the European Union showing no change.  
326 We caution that these trends are most uncertain before 2000 and in regions with few  
327 observations; under these conditions our estimated trends mainly reflect models and a small  
328 number of observations. Year-to-year changes in ozone in regions with few observations may  
329 also result from using different model weights in individual years. These trends are supported by  
330 a previous analysis of TOAR data for 2000–2014 summertime ozone, which found a positive  
331 trend in East Asia and negative trends in North America and Europe.<sup>57</sup> Similarly, a study of

332 CNEMC observations showed increases in China for 2013–2017.<sup>31</sup> One study suggests that the  
333 2013-2017 increase over China was influenced most by the decrease of PM<sub>2.5</sub>, which increased  
334 HO<sub>x</sub> radicals<sup>58</sup>; therefore, a PM<sub>2.5</sub> increase might explain our estimated 2007-2013 ozone  
335 decrease. Increasing trends in other regions with few observations, including Africa and South  
336 Central Asia are supported by long-term aircraft<sup>59</sup> and satellite column observations.<sup>47</sup>



337

338 **Figure 5.** (a) Percent of the global population exposed to 10 ppb intervals of OSDMA8 from  
 339 1990-2017. (b) Ozone trend regionally (regions defined in Figure S1) over 1990–2017 for the  
 340 metric of population weighted OSDMA8. All trends have p-values less than 0.05, except for  
 341 Europe and South America (Table S3). Uncertainty intervals are included in Figures S33-46.

342 **DISCUSSION**

343           We create fine resolution yearly ozone distributions for 1990–2017 that incorporate  
344 surface observations and output from nine atmospheric chemistry models, using a novel  
345 combination of the M<sup>3</sup>Fusion method for creating a multi-model composite, which dominates the  
346 large-scale ozone estimates, and BME data fusion which influences ozone estimates near  
347 observation locations, smoothly integrating observations in space and time. Our analysis finds  
348 that methods incorporating observations outperform ozone estimated from models only.  
349 Additionally, the influence of an observation across multiple years in BME further improves our  
350 ozone estimate. Our method’s major strengths include the incorporation of multiple data types,  
351 the smooth weighting of observational influence across space and time, the ability to output a  
352 variance at every estimation point, and the estimation of global ozone with fine spatial structure.  
353 The improvement in model performance from using our combination of M<sup>3</sup>Fusion and BME  
354 provides a caution against using simple spatial interpolations of observations or output of a  
355 model without bias correction, to represent ozone. Although we improve upon the previous  
356 GBD ozone estimate, some limitations remain. The lack of monitoring stations in large populous  
357 regions limits our abilities to understand ozone exposure in these areas, where these uncertainties  
358 affect both the multi-model composite and BME data fusion. Our method is limited in years with  
359 fewer observations and models available; additionally, the fine resolution model output that  
360 informs the fine spatial pattern of our output is only available for a single year. Future work may  
361 apply a nonlinear bias correction, or use machine learning to correct bias,<sup>60</sup> to the multi-model  
362 composite to improve the global offset, and thus the overall estimation. Our work also shows the  
363 value of using multiple models in creating a multi-model composite, as output from each model  
364 was selected (weight>0) in at least some regions and years.

365 Our method can be applied to future years as more observations and model output  
366 become available. Additionally, our method can be used to estimate ozone metrics other than  
367 OSDMA8, including for studies of vegetation and crop impacts.<sup>61</sup> While model output and  
368 geostatistical techniques like BME can estimate global ozone, estimates suffer from the lack of  
369 observations in some world regions. Additional observations, especially in unmonitored regions  
370 with large populations including megacities in low- and middle-income nations, are essential to  
371 improve understanding of ozone exposure and health burden.

372 Ozone exposure is increasing globally, with global population-weighted ozone showing a  
373 positive trend from 1990-2017, driven by strong positive trends in highly populated and polluted  
374 regions of Asia and Africa. The increasing global exposure to ozone indicates that current ozone  
375 management policies are failing to reduce ozone exposure in many regions of the world. Our  
376 results can be used by policy makers to identify regions where ozone pollution could be  
377 mitigated through reductions of ozone precursor emissions, mainly from fossil-fuel combustion,  
378 on local, national and continental scales, or through international agreements to reduce  
379 emissions, including methane, that affect global background ozone.<sup>62,63</sup>

## 380 **ASSOCIATED CONTENT**

381 **Supporting Information.** The supporting information includes multi-model composite model  
382 weights, covariance parameters, fine resolution addition example, yearly maps for all relevant  
383 scenarios, cross validation statistics, and national ozone trends with uncertainty intervals.

## 384 **AUTHOR INFORMATION**

385 Corresponding Author: J. Jason West, [jasonwest@unc.edu](mailto:jasonwest@unc.edu), 919-843-3928.

## 386 **ACKNOWLEDGEMENTS**



387 We acknowledge support from the NASA Health and Air Quality Applied Sciences Team  
388 (#NNX16AQ30G) and the National Institute for Occupational Safety and Health (T42-  
389 OH008673). Makoto Deushi was supported by the Japan Society for the Promotion of Science  
390 (JP20K04070).

391

## 392 REFERENCES

- 393 (1) Jerrett, M.; Burnett, R. T.; Arden Pope, C.; Ito, K.; Thurston, G.; Krewski, D.; Shi, Y.;  
394 Calle, E.; Thun, M. Long-Term Ozone Exposure and Mortality. *N. Engl. J. Med.* **2009**,  
395 *360* (11), 1085–1095. <https://doi.org/10.1056/NEJMoa0803894>.
- 396 (2) Turner, M. C.; Jerrett, M.; Pope, C. A.; Krewski, D.; Gapstur, S. M.; Diver, W. R.;  
397 Beckerman, B. S.; Marshall, J. D.; Su, J.; Crouse, D. L.; Burnett, R. T. Long-Term Ozone  
398 Exposure and Mortality in a Large Prospective Study. *Am. J. Respir. Crit. Care Med.*  
399 **2016**, *193* (10), 1134–1142. <https://doi.org/10.1164/rccm.201508-1633OC>.
- 400 (3) Di, Q.; Dai, L.; Wang, Y.; Zanobetti, A.; Choirat, C.; Schwartz, J. D.; Dominici, F.  
401 Association of short-term exposure to air pollution with mortality in older adults, *J. Amer.*  
402 *Med. Assoc.* **2017**, *318* (24), 2446-2456. doi: 10.1001/jama.2017.17923.(4) Myhre, G.,  
403 Shindell, D., Bréon, F.-M., Collins, W., Fuglestedt, J., Huang, J., Koch, D., Lamarque,  
404 J.-F., Lee, D., Mendoza, B., et al. Anthropogenic and Natural Radiative Forcing. In:  
405 Climate Change 2013: The Physical Science Basis. Contribution of Working Group I to  
406 the Fifth Assessment Report of the Intergovernmental Panel on Climate Change [Stocker,  
407 T.F., D. Qin, G.-K. Plattner, M. Ti; Cambridge University Press: Cambridge, United  
408 Kingdom and New York, NY, USA, 2013.
- 409 (5) U.S. EPA. *Integrated Science Assessment for Ozone and Related Photochemical*

- 410 *Oxidants*; U.S. Environmental Protection Agency, Washington, DC, EPA/600/R-20/012,  
411 2020.
- 412 (6) Emberson, L. D.; Pleijel, H.; Ainsworth, E. A.; van den Berg, M.; Ren, W.; Osborne, S.;  
413 Mills, G.; Pandey, D.; Dentener, F.; Büker, P.; et al. Ozone Effects on Crops and  
414 Consideration in Crop Models. *Eur. J. Agron.* **2018**, *100*, 19–34.  
415 <https://doi.org/10.1016/j.eja.2018.06.002>.
- 416 (7) Fleming, Z. L.; Doherty, R. M.; Von Schneidmesser, E.; Malley, C. S.; Cooper, O. R.;  
417 Pinto, J. P.; Colette, A.; Xu, X.; Simpson, D.; Schultz, M. G.; et al. Tropospheric Ozone  
418 Assessment Report: Present-Day Ozone Distribution and Trends Relevant to Human  
419 Health. *Elementa* **2018**, *6* (1). <https://doi.org/10.1525/elementa.273>.
- 420 (8) Cooper, O. R.; Parrish, D. D.; Ziemke, J.; Balashov, N. V.; Cupeiro, M.; Galbally, I. E.;  
421 Gilge, S.; Horowitz, L.; Jensen, N. R.; Lamarque, J.-F.; et al. Global Distribution and  
422 Trends of Tropospheric Ozone: An Observation-Based Review. *Elem. Sci. Anthr.* **2014**, *2*  
423 (0), 000029. <https://doi.org/10.12952/journal.elementa.000029>.
- 424 (9) Lim, S. S.; Vos, T.; Flaxman, A. D.; Danaei, G.; Shibuya, K.; Adair-Rohani, H.; Amann,  
425 M.; Anderson, H. R.; Andrews, K. G.; Aryee, M.; et al. A Comparative Risk Assessment  
426 of Burden of Disease and Injury Attributable to 67 Risk Factors and Risk Factor Clusters  
427 in 21 Regions, 1990-2010: A Systematic Analysis for the Global Burden of Disease Study  
428 2010. *Lancet* **2012**, *380* (9859), 2224–2260. [https://doi.org/10.1016/S0140-](https://doi.org/10.1016/S0140-6736(12)61766-8)  
429 [6736\(12\)61766-8](https://doi.org/10.1016/S0140-6736(12)61766-8).
- 430 (10) Cohen, A. J.; Brauer, M.; Burnett, R.; Anderson, H. R.; Frostad, J.; Estep, K.;  
431 Balakrishnan, K.; Brunekreef, B.; Dandona, L.; Dandona, R.; et al. Estimates and 25-Year  
432 Trends of the Global Burden of Disease Attributable to Ambient Air Pollution: An

- 433 Analysis of Data from the Global Burden of Diseases Study 2015. *Lancet* **2017**, 389  
434 (10082), 1907–1918. [https://doi.org/10.1016/S0140-6736\(17\)30505-6](https://doi.org/10.1016/S0140-6736(17)30505-6).
- 435 (11) Shaddick, G.; Thomas, M. L.; Green, A.; Brauer, M.; van Donkelaar, A.; Burnett, R.;  
436 Chang, H. H.; Cohen, A.; Dingenen, R. Van; Dora, C.; et al. Data Integration Model for  
437 Air Quality: A Hierarchical Approach to the Global Estimation of Exposures to Ambient  
438 Air Pollution. *J. R. Stat. Soc. Ser. C Appl. Stat.* **2018**, 67 (1), 231–253.  
439 <https://doi.org/10.1111/rssc.12227>.
- 440 (12) Shaddick, G.; Thomas, M. L.; Amini, H.; Broday, D.; Cohen, A.; Frostad, J.; Green, A.;  
441 Gumy, S.; Liu, Y.; Martin, R. V.; et al. Data Integration for the Assessment of Population  
442 Exposure to Ambient Air Pollution for Global Burden of Disease Assessment. *Environ.*  
443 *Sci. Technol.* **2018**, 52 (16), 9069–9078. <https://doi.org/10.1021/acs.est.8b02864>.
- 444 (13) Stanaway, J. D.; Afshin, A.; Gakidou, E.; Lim, S. S.; Abate, D.; Abate, K. H.; Abbafati,  
445 C.; Abbasi, N.; Abbastabar, H.; Abd-Allah, F.; et al. Global, Regional, and National  
446 Comparative Risk Assessment of 84 Behavioural, Environmental and Occupational, and  
447 Metabolic Risks or Clusters of Risks for 195 Countries and Territories, 1990–2017: A  
448 Systematic Analysis for the Global Burden of Disease Study 2017. *Lancet* **2018**, 392  
449 (10159), 1923–1994. [https://doi.org/10.1016/S0140-6736\(18\)32225-6](https://doi.org/10.1016/S0140-6736(18)32225-6).
- 450 (14) Brauer, M.; Freedman, G.; Frostad, J.; Van Donkelaar, A.; Martin, R. V.; Dentener, F.;  
451 Dingenen, R. Van; Estep, K.; Amini, H.; Apte, J. S.; et al. Ambient Air Pollution  
452 Exposure Estimation for the Global Burden of Disease 2013. *Environ. Sci. Technol.* **2016**,  
453 50 (1), 79–88. <https://doi.org/10.1021/acs.est.5b03709>.
- 454 (15) Gaudel, A.; Cooper, O. R.; Ancellet, G.; Barret, B.; Boynard, A.; Burrows, J. P.;  
455 Clerbaux, C.; Coheur, P. F.; Cuesta, J.; Cuevas, E.; et al. Tropospheric Ozone Assessment

- 456 Report: Present-Day Distribution and Trends of Tropospheric Ozone Relevant to Climate  
457 and Global Atmospheric Chemistry Model Evaluation. *Elementa* **2018**, 6 (1).  
458 <https://doi.org/10.1525/elementa.291>.
- 459 (16) Schultz, M. G.; Schröder, S.; Lyapina, O.; Cooper, O.; Galbally, I.; Petropavlovskikh, I.;  
460 Von Schneidmesser, E.; Tanimoto, H.; Elshorbany, Y.; Naja, M.; et al. Tropospheric  
461 Ozone Assessment Report: Database and Metrics Data of Global Surface Ozone  
462 Observations. *Elem Sci Anth* **2017**, 5 (0), 58. <https://doi.org/10.1525/elementa.244>.
- 463 (17) Morgenstern, O.; Hegglin, M.; Rozanov, E.; O'Connor, F.; Luke Abraham, N.; Akiyoshi,  
464 H.; Archibald, A.; Bekki, S.; Butchart, N.; Chipperfield, M.; et al. Review of the Global  
465 Models Used within Phase 1 of the Chemistry-Climate Model Initiative (CCMI).  
466 *Geoscientific Model Development*. Copernicus GmbH February 13, 2017, pp 639–671.  
467 <https://doi.org/10.5194/gmd-10-639-2017>.
- 468 (18) Chang, K.-L.; Cooper, O. R.; West, J. J.; Serre, M. L.; Schultz, M. G.; Lin, M.; Marécal,  
469 V.; Josse, B.; Deushi, M.; Sudo, K.; et al. A New Method (M<sup>3</sup> Fusion v1) for Combining  
470 Observations and Multiple Model Output for an Improved Estimate of the Global Surface  
471 Ozone Distribution. *Geosci. Model Dev.* **2019**, 12 (3), 955–978.  
472 <https://doi.org/10.5194/gmd-12-955-2019>.
- 473 (19) Christakos, G. A Bayesian/Maximum-Entropy View to the Spatial Estimation Problem.  
474 *Math. Geol.* **1990**, 22 (7), 763–777. <https://doi.org/10.1007/BF00890661>.
- 475 (20) Christakos, G.; Bogaert, P.; Serre, M. L. *Temporal GIS: Advanced Functions for Field-*  
476 *Based Applications*; Springer Berlin Heidelberg, 2001.
- 477 (21) Serre, M. L.; Christakos, G. Modern Geostatistics: Computational BME Analysis in the  
478 Light of Uncertain Physical Knowledge - The Equus Beds Study. *Stoch. Environ. Res.*

- 479 *Risk Assess.* **1999**, *13* (1–2), 1–26. <https://doi.org/10.1007/s004770050029>.
- 480 (22) Christakos, G.; Kolovos, A.; Serre, M. L.; Vukovich, F. Total Ozone Mapping by  
481 Integrating Databases from Remote Sensing Instruments and Empirical Models. *IEEE*  
482 *Trans. Geosci. Remote Sens.* **2004**, *42* (5), 991–1008.  
483 <https://doi.org/10.1109/TGRS.2003.822751>.
- 484 (23) Nazelle, A. De; Arunachalam, S.; Serre, M. L. Bayesian Maximum Entropy Integration of  
485 Ozone Observations and Model Predictions: An Application for Attainment  
486 Demonstration in North Carolina. *Environ. Sci. Technol.* **2010**, *44* (15), 5707–5713.  
487 <https://doi.org/10.1021/es100228w>.
- 488 (24) Xu, Y.; Serre, M. L.; Reyes, J.; Vizuete, W. Bayesian Maximum Entropy Integration of  
489 Ozone Observations and Model Predictions: A National Application. *Environ. Sci.*  
490 *Technol.* **2016**, *50* (8), 4393–4400. <https://doi.org/10.1021/acs.est.6b00096>.
- 491 (25) Xu, Y.; Serre, M. L.; Reyes, J. M.; Vizuete, W. Impact of Temporal Upscaling and  
492 Chemical Transport Model Horizontal Resolution on Reducing Ozone Exposure  
493 Misclassification. *Atmos. Environ.* **2017**, *166*, 374–382.  
494 <https://doi.org/10.1016/j.atmosenv.2017.07.033>.
- 495 (26) Hu, L.; Keller, C. A.; Long, M. S.; Sherwen, T.; Auer, B.; Da Silva, A.; Nielsen, J. E.;  
496 Pawson, S.; Thompson, M. A.; Trayanov, A. L.; et al. Global Simulation of Tropospheric  
497 Chemistry at 12.5&Thinsp;Km Resolution: Performance and Evaluation of the  
498 GEOS-Chem Chemical Module (V10-1) within the NASA GEOS Earth System Model  
499 (GEOS-5 ESM). *Geosci. Model Dev.* **2018**, *11* (11), 4603–4620.  
500 <https://doi.org/10.5194/gmd-11-4603-2018>.
- 501 (27) Murray, C. J. L.; Aravkin, A. Y.; Zheng, P.; Abbafati, C.; Abbas, K. M.; Abbasi-

502 Kangevari, M.; Abd-Allah, F.; Abdelalim, A.; Abdollahi, M.; Abdollahpour, I.; et al.  
503 Global Burden of 87 Risk Factors in 204 Countries and Territories, 1990–2019: A  
504 Systematic Analysis for the Global Burden of Disease Study 2019. *Lancet* **2020**, *396*  
505 (10258), 1223–1249. [https://doi.org/10.1016/S0140-6736\(20\)30752-2](https://doi.org/10.1016/S0140-6736(20)30752-2).(28) Seltzer, K. M.;  
506 Shindell, D. T.; Kasibhatla, P.; Malley, C. S. Magnitude, Trends, and Impacts of Ambient  
507 Long-Term Ozone Exposure in the United States from 2000 to 2015. *Atmos. Chem. Phys.*  
508 **2020**, *20* (3), 1757–1775. <https://doi.org/10.5194/acp-20-1757-2020>.

509 (29) Kleinert, F.; Leufen, L.; Schultz, M. IntelliO3-Ts v1.0: A Neural Network Approach to  
510 Predict near-Surface Ozone Concentrations in Germany. *Geosci. Model Dev. Discuss.*  
511 **2020**, 1–69. <https://doi.org/10.5194/gmd-2020-169>.

512 (30) Schultz, Martin G; Schröder, Sabine; Lyapina, Olga; Cooper, Owen R; Galbally, Ian;  
513 Petropavlovskikh, Irina; von Schneidemesser, Erika; Tanimoto, Hiroshi; Elshorbany,  
514 Yasin; Naja, Manish; et al. Tropospheric Ozone Assessment Report, Links to Global  
515 Surface Ozone Datasets. *PANGAEA* **2017**.

516 (31) Lu, X.; Hong, J.; Zhang, L.; Cooper, O. R.; Schultz, M. G.; Xu, X.; Wang, T.; Gao, M.;  
517 Zhao, Y.; Zhang, Y. Severe Surface Ozone Pollution in China: A Global Perspective.  
518 *Environ. Sci. Technol. Lett.* **2018**, *5* (8), 487–494.  
519 <https://doi.org/10.1021/acs.estlett.8b00366>.

520 (32) Orbe, C.; Plummer, D. A.; Waugh, D. W.; Yang, H.; Jöckel, P.; Kinnison, D. E.; Josse, B.;  
521 Marecal, V.; Deushi, M.; Abraham, N. L.; et al. Description and Evaluation of the  
522 Specified-Dynamics Experiment in the Chemistry-Climate Model Initiative. *Atmos. Chem.*  
523 *Phys.* **2020**, *20* (6), 3809–3840. <https://doi.org/10.5194/acp-20-3809-2020>.

524 (33) Lamarque, J.-F.; Bond, T. C.; Eyring, V.; Granier, C.; Heil, A.; Klimont, Z.; Lee, D.;

525 Lioussé, C.; Mieville, A.; Owen, B.; et al. Historical (1850–2000) Gridded Anthropogenic  
526 and Biomass Burning Emissions of Reactive Gases and Aerosols: Methodology and  
527 Application. *Atmos. Chem. Phys.* **2010**, *10* (15), 7017–7039. [https://doi.org/10.5194/acp-](https://doi.org/10.5194/acp-10-7017-2010)  
528 [10-7017-2010](https://doi.org/10.5194/acp-10-7017-2010).

529 (34) Granier, C.; Bessagnet, B.; Bond, T.; D’Angiola, A.; van der Gon, H. D.; Frost, G. J.;  
530 Heil, A.; Kaiser, J. W.; Kinne, S.; Klimont, Z.; et al. Evolution of Anthropogenic and  
531 Biomass Burning Emissions of Air Pollutants at Global and Regional Scales during the  
532 1980-2010 Period. *Clim. Change* **2011**, *109* (1), 163–190. [https://doi.org/10.1007/s10584-](https://doi.org/10.1007/s10584-011-0154-1)  
533 [011-0154-1](https://doi.org/10.1007/s10584-011-0154-1).

534 (35) Eyring, V.; Bony, S.; Meehl, G. A.; Senior, C. A.; Stevens, B.; Stouffer, R. J.; Taylor, K.  
535 E. Overview of the Coupled Model Intercomparison Project Phase 6 (CMIP6)  
536 Experimental Design and Organization. *Geosci. Model Dev.* **2016**, *9* (5), 1937–1958.  
537 <https://doi.org/10.5194/gmd-9-1937-2016>.

538 (36) Tilmes, S.; Lamarque, J.-F.; Emmons, L. K.; Kinnison, D. E.; Ma, P.-L.; Liu, X.; Ghan,  
539 S.; Bardeen, C.; Arnold, S.; Deeter, M.; et al. Description and Evaluation of Tropospheric  
540 Chemistry and Aerosols in the Community Earth System Model (CESM1.2). *Geosci.*  
541 *Model Dev.* **2015**, *8* (5), 1395–1426. <https://doi.org/10.5194/gmd-8-1395-2015>.

542 (37) Garcia, R. R.; Smith, A. K.; Kinnison, D. E.; de la Cámara, Á.; Murphy, D. J.  
543 Modification of the Gravity Wave Parameterization in the Whole Atmosphere Community  
544 Climate Model: Motivation and Results. *J. Atmos. Sci.* **2017**, *74* (1), 275–291.  
545 <https://doi.org/10.1175/JAS-D-16-0104.1>.

546 (38) Marsh, D. R.; Mills, M. J.; Kinnison, D. E.; Lamarque, J. F.; Calvo, N.; Polvani, L. M.  
547 Climate Change from 1850 to 2005 Simulated in CESM1(WACCM). *J. Clim.* **2013**, *26*

- 548 (19), 7372–7391. <https://doi.org/10.1175/JCLI-D-12-00558.1>.
- 549 (39) Sudo, K.; Takahashi, M.; Kurokawa, J.; Akimoto, H. CHASER: A Global Chemical  
550 Model of the Troposphere 1. Model Description. *J. Geophys. Res. Atmos.* **2002**, *107*  
551 (D17), ACH 7-1-ACH 7-20. <https://doi.org/10.1029/2001JD001113>.
- 552 (40) Sudo, K.; Takahashi, M.; Akimoto, H. CHASER: A Global Chemical Model of the  
553 Troposphere 2. Model Results and Evaluation. *J. Geophys. Res. Atmos.* **2002**, *107* (D21),  
554 ACH 9-1-ACH 9-39. <https://doi.org/10.1029/2001JD001114>.
- 555 (41) Watanabe, S.; Hajima, T.; Sudo, K.; Nagashima, T.; Takemura, T.; Okajima, H.; Nozawa,  
556 T.; Kawase, H.; Abe, M.; Yokohata, T.; et al. MIROC-ESM 2010: Model Description and  
557 Basic Results of CMIP5-20c3m Experiments. *Geosci. Model Dev.* **2011**, *4* (4), 845–872.  
558 <https://doi.org/10.5194/gmd-4-845-2011>.
- 559 (42) Lin, M.; Fiore, A. M.; Horowitz, L. W.; Cooper, O. R.; Naik, V.; Holloway, J.; Johnson,  
560 B. J.; Middlebrook, A. M.; Oltmans, S. J.; Pollack, I. B.; et al. Transport of Asian Ozone  
561 Pollution into Surface Air over the Western United States in Spring. *J. Geophys. Res.*  
562 *Atmos.* **2012**, *117* (4). <https://doi.org/10.1029/2011JD016961>.
- 563 (43) Lin, M.; Horowitz, L. W.; Oltmans, S. J.; Fiore, A. M.; Fan, S. Tropospheric Ozone  
564 Trends at Mauna Loa Observatory Tied to Decadal Climate Variability. *Nat. Geosci.*  
565 **2014**, *7* (2), 136–143. <https://doi.org/10.1038/ngeo2066>.
- 566 (44) Lin, M.; Horowitz, L. W.; Payton, R.; Fiore, A. M.; Tonnesen, G. US Surface Ozone  
567 Trends and Extremes from 1980 to 2014: Quantifying the Roles of Rising Asian  
568 Emissions, Domestic Controls, Wildfires, and Climate. *Atmos. Chem. Phys.* **2017**, *17* (4),  
569 2943–2970. <https://doi.org/10.5194/acp-17-2943-2017>.
- 570 (45) Zhang, L.; Lin, M.; Langford, A.; Horowitz, L.; Senff, C.; Klovenski, E.; Wang, Y.;



- 571 Alvarez II, R.; Petropavlovskikh, I.; Cullis, P.; et al. Characterizing Sources of High  
572 Surface Ozone Events in the Southwestern U.S. with Intensive Field Measurements and  
573 Two Global Models. *Atmos. Chem. Phys.* **2019**, 1–47. [https://doi.org/10.5194/acp-2019-](https://doi.org/10.5194/acp-2019-990)  
574 990.
- 575 (46) Horowitz, L. W., Naik, V., Paulot, F., Ginoux, P., Dunne, J. P., Mao, J. Q., et al. The  
576 GFDL Global Atmospheric Chemistry-Climate Model AM4.1: Model Description and  
577 Simulation Characteristics. *J. Adv. Model. Earth Syst.* **2020**, *submitted*.
- 578 (47) Ziemke, J. R.; Oman, L. D.; Strode, S. A.; Douglass, A. R.; Olsen, M. A.; McPeters, R.  
579 D.; Bhartia, P. K.; Froidevaux, L.; Labow, G. J.; Witte, J. C.; et al. Trends in Global  
580 Tropospheric Ozone Inferred from a Composite Record of TOMS/OMI/MLS/OMPS  
581 Satellite Measurements and the MERRA-2 GMI Simulation. *Atmos. Chem. Phys.* **2019**, *19*  
582 (5), 3257–3269. <https://doi.org/10.5194/acp-19-3257-2019>.
- 583 (48) Strode, S. A.; Ziemke, J. R.; Oman, L. D.; Lamsal, L. N.; Olsen, M. A.; Liu, J. Global  
584 Changes in the Diurnal Cycle of Surface Ozone. *Atmos. Environ.* **2019**, *199*, 323–333.  
585 <https://doi.org/10.1016/j.atmosenv.2018.11.028>.
- 586 (49) Josse, B.; Simon, P.; Peuch, V.-H. Radon Global Simulations with the Multiscale  
587 Chemistry and Transport Model MOCAGE. *Tellus B Chem. Phys. Meteorol.* **2004**, *56* (4),  
588 339–356. <https://doi.org/10.3402/tellusb.v56i4.16448>.
- 589 (50) Teyssède, H.; Michou, M.; Clark, H. L.; Josse, B.; Karcher, F.; Olivie, D.; Peuch, V.-H.;  
590 Saint-Martin, D.; Cariolle, D.; Attié, J.-L.; et al. New Tropospheric and Stratospheric  
591 Chemistry and Transport Model MOCAGE-Climat for Multi-Year Studies: Evaluation of  
592 the Present-Day Climatology and Sensitivity to Surface Processes. *Atmos. Chem. Phys.*  
593 **2007**, *7* (22), 5815–5860. <https://doi.org/10.5194/acp-7-5815-2007>.

- 594 (51) Adachi, Y.; Yukimoto, S.; Deushi, M.; Obata, A.; Nakano, H.; Tanaka, T. Y.; Hosaka, M.;  
595 Sakami, T.; Yoshimura, H.; Hirabara, M.; et al. Basic Performance of a New Earth System  
596 Model of the Meteorological Research Institute. *Pap. Meteorol. Geophys.* **2013**, *64*, 1–19.  
597 <https://doi.org/10.2467/mripapers.64.1>.
- 598 (52) Yukimoto, S.; Kawai, H.; Koshiro, T.; Oshima, N.; Yoshida, K.; Urakawa, S.; Tsujino, H.;  
599 Deushi, M.; Tanaka, T.; Hosaka, M.; et al. The Meteorological Research Institute Earth  
600 System Model Version 2.0, MRI-ESM2.0: Description and Basic Evaluation of the  
601 Physical Component. *J. Meteorol. Soc. Japan* **2019**, *97* (5), 931–965.  
602 <https://doi.org/10.2151/jmsj.2019-051>.
- 603 (53) Bolin, D.; Lindgren, F. Spatial Models Generated by Nested Stochastic Partial Differential  
604 Equations, with an Application to Global Ozone Mapping. *Ann. Appl. Stat.* **2011**, *5* (1),  
605 523–550. <https://doi.org/10.1214/10-AOAS383>.
- 606 (54) Christakos, G. *Modern Spatiotemporal Geostatistics*; Oxford University Press: Cary, NC,  
607 2000.
- 608 (55) Freire, L. S.; Gerken, T.; Ruiz-Plancarte, J.; Wei, D.; Fuentes, J. D.; Katul, G. G.; Dias, N.  
609 L.; Acevedo, O. C.; Chamecki, M. Turbulent Mixing and Removal of Ozone within an  
610 Amazon Rainforest Canopy. *J. Geophys. Res. Atmos.* **2017**, *122* (5), 2791–2811.  
611 <https://doi.org/10.1002/2016JD026009>.
- 612 (56) Bauer, S. E.; Im, U.; Mezuman, K.; Gao, C. Y. Desert Dust, Industrialization, and  
613 Agricultural Fires: Health Impacts of Outdoor Air Pollution in Africa. *J. Geophys. Res.*  
614 *Atmos.* **2019**, *124* (7), 4104–4120. <https://doi.org/10.1029/2018JD029336>.
- 615 (57) Chang, K.-L.; Petropavlovskikh, I.; Copper, O. R.; Schultz, M. G.; Wang, T. Regional  
616 Trend Analysis of Surface Ozone Observations from Monitoring Networks in Eastern

617 North America, Europe and East Asia. *Elem Sci Anth* **2017**, 5 (0), 50.  
618 <https://doi.org/10.1525/elementa.243>.

619 (58) Li, K.; Jacob, D. J.; Liao, H.; Shen, L.; Zhang, Q.; Bates, K. H. Anthropogenic Drivers of  
620 2013–2017 Trends in Summer Surface Ozone in China. *Proc. Natl. Acad. Sci. U. S. A.*  
621 **2019**, 116 (2), 422–427. <https://doi.org/10.1073/pnas.1812168116>.

622 (59) Gaudel, A.; Cooper, O. R.; Chang, K. L.; Bourgeois, I.; Ziemke, J. R.; Strode, S. A.;  
623 Oman, L. D.; Sellitto, P.; Nédélec, P.; Blot, R.; et al. Aircraft Observations since the  
624 1990s Reveal Increases of Tropospheric Ozone at Multiple Locations across the Northern  
625 Hemisphere. *Sci. Adv.* **2020**, 6 (34). <https://doi.org/10.1126/sciadv.aba8272>.

626 (60) Ivatt, P. D.; Evans, M. J. Improving the Prediction of an Atmospheric Chemistry  
627 Transport Model Using Gradient-Boosted Regression Trees. *Atmos. Chem. Phys.* **2020**, 20  
628 (13), 8063–8082. <https://doi.org/10.5194/acp-20-8063-2020>.

629 (61) Mills, G.; Pleijel, H.; Malley, C. S.; Sinha, B.; Cooper, O. R.; Schultz, M. G.; Neufeld, H.  
630 S.; Simpson, D.; Sharps, K.; Feng, Z.; et al. Tropospheric Ozone Assessment Report:  
631 Present-Day Tropospheric Ozone Distribution and Trends Relevant to Vegetation.  
632 *Elementa* **2018**, 6 (1). <https://doi.org/10.1525/elementa.302>.

633 (62) West, J. J.; Fiore, A. M.; Horowitz, L. W.; Mauzerall, D. L. Global Health Benefits of  
634 Mitigating Ozone Pollution with Methane Emission Controls. *Proc. Natl. Acad. Sci. U. S.*  
635 *A.* **2006**, 103 (11), 3988–3993. <https://doi.org/10.1073/pnas.0600201103>.

636 (63) Dentener, F.; Keating, T.; Akimoto, H. *Hemispheric Transport of Air Pollution: Part A:*  
637 *Ozone and Particulate Matter*; Economic Commission for Europe, Geneva, 2010.  
638